Observed variability of north atlantic oceanic precipitating systems during winter

Jean-Pierre Chaboureau, Chantal Claud

JOURNAL OF GEOPHYSICAL RESEARCH, VOL. 108, NO. D14, 4435, doi:10.1029/2002JD003343, 2003

Observed variability of North Atlantic oceanic precipitating systems during winter

Jean-Pierre Chaboureau
Laboratoire d'Aérologie, Observatoire Midi-Pyrénées, Toulouse, France

Chantal Claud
Laboratoire de Météorologie Dynamique, École Polytechnique, Palaiseau, France

Received 20 December 2002; revised 28 March 2003; accepted 2 April 2003; published 31 July 2003.

[1] The variability of large precipitating weather systems as observed from polar satellites over the North Atlantic Ocean is investigated using a statistical analysis. Nine winters (from 1987 to 1995) have been considered. Cloud systems and troughs over the area 40–60°N, 70–10°W are automatically detected with retrievals of the cloud top pressure, a precipitation index, and the temperature of the lower stratosphere. A classification of the largest precipitating systems as characterized by these variables leads to eight classes, whose occurrence significantly differs over the years. It also shows the systematic presence of a trough upstream of the precipitating area covered by high-level clouds, as expected in the case of baroclinic interaction. In order to understand the large interannual variability an attempt to identify systematic differences in cyclone structures during different flow regimes is then performed. It shows that the large-scale (typically 3000 km wide) and zonally elongated cloud systems are observed mainly to the south of 45°N when the phase of the Arctic Oscillation (AO) is negative (which also corresponds to the Greenland Anticyclone regime). Conversely, zonally elongated cloud systems of smaller scale (1000 km wide) associated with frontal waves are favored also to the south but during the positive AO phase (particularly during zonal regimes). The most tilted weather systems, without any preferential AO phase, are found mostly during the blocking regime. These systems are cyclonically tilted in the northeastern branch of the storm track and anticyclonically tilted in the southwestern branch. It must be noted that similar results are obtained when the AO daily index is replaced by the North Atlantic Oscillation index. This analysis gives observational evidence of previous idealized simulations linking the large-scale circulation to preferential life cycles of weather systems. In addition, a weak response to extreme El Niño Southern Oscillation events has been observed in the location of cyclones but not in their average structure. *INDEX TERMS:* 3309 Meteorology and Atmospheric Dynamics: Climatology (1620); 3354 Meteorology and Atmospheric Dynamics: Precipitation (1854); 3360 Meteorology and Atmospheric Dynamics: Remote sensing; 3364 Meteorology and Atmospheric Dynamics: Synoptic-scale meteorology; *KEYWORDS:* satellite observation, precipitating weather system, interannual variability, North Atlantic Oscillation, weather regime

Citation: Chaboureau, J.-P., and C. Claud, Observed variability of North Atlantic oceanic precipitating systems during winter, *J. Geophys. Res.*, *108*(D14), 4435, doi:10.1029/2002JD003343, 2003.

1. Introduction

[2] The North Atlantic region is one of the most frequent storm occurrence regions, especially during the wintertime. These storms have a strong influence on the everyday life of millions of people and as such represent a challenge in terms of forecasting but are also closely linked with climate variability and change. It is therefore crucial not only to have a good knowledge of the morphology of the storms but also to understand the links between this morphology and the large-scale circulation. The present work represents an effort toward this goal.

[3] There has been in the past a number of climatic studies devoted to precipitating systems over the North Atlantic during wintertime. Most of them relied on reanalyses and, more specifically, on the European Centre for Medium-Range Weather Forecasts (ECMWF) project [e.g., *Sickmöller et al.*, 2000] or the National Centers for Environmental Prediction (NCEP) National Center for Atmospheric Research (NCAR) project [e.g., *Geng and Sugi*, 2001; *Paciorek et al.*, 2002] or both [*Hoskins and Hodges*, 2002]. Through cyclone identification and tracking techniques, these studies concentrate on the dynamical aspect of

0148-0227/03/2002JD003343

extratropical cyclones, the storm-tracks, and the long-term trends in cyclone activity.

[4] On the other hand, climatological studies based on satellite observations, which give insight into the cloud structure, are rather rare. An exception is due to [*Evans et al.*, 1994], who performed a subjective classification of cloud imagery for an ensemble of 50 cases of explosive cyclogenesis that occurred during the 1970s and 1980s in the western North Atlantic region. More recently, a study using the International Satellite Cloud Climatology Project (ISCCP) data set examines the relation between several composites of clouds with the largest optical thickness and the large-scale circulation from the ECMWF analyses [*Lau and Crane*, 1995]. Results for the midlatitude composite show consistency of the ISCPP cloud patterns with the atmospheric flow.

[5] In this study, we examine midlatitude weather systems through their signature on the water budget (cloud and precipitation) using physical parameters retrieved from the measurements of the TIROS-N Operational Vertical Sounder (TOVS) onboard National Oceanic and Atmospheric Administration (NOAA) satellites. These retrievals are the cloud top pressure, a precipitation index and the so-called temperature of the lower stratosphere (TLS), which represents the temperature around the tropopause. In a previous work, *Chaboureau et al.* [2001] have shown that these retrievals can be used to characterize weather regimes. This previous study was conducted over a 2-month period which corresponded to the FASTEX (the Fronts and Atlantic Storm Track Experiment) campaign. Here it is extended to a nine winter period.

[6] In addition, *Chaboureau et al.* [2001] performed a composite study on the weather systems with the largest precipitation signature and the obtained typology suggested that classes associated with blocking and zonal regimes lead to preferential baroclinic life cycles that mimic the life cycle 1 (LC1) and life cycle 2 (LC2) paradigms, respectively [*Thorncroft et al.*, 1993]. This terminology stems from idealized simulations which have shown a preferential life cycle according to the small meridional barotropic shear superimposed on the symmetric baroclinic jet [e.g., *Hoskins*, 1990; *Davies et al.*, 1991; *Thorncroft et al.*, 1993; *Wernli et al.*, 1998]. Without barotropic shear, cyclones develop as life cycle 1 (LC1) into warm-frontal cyclones and are characterized by backward tilted, thinning troughs being advected anticyclonically. Conversely, within barotropic sheared environment, cyclones evolve through a life cycle 2 (LC2) into occluded cyclones, characterized by forward tilted, broadening troughs wrapping themselves up cyclonically. The influence of planetary-scale flow on life cycles of precipitating systems have been also analysed in simulations of actual life cycles of a few north Atlantic cases. The LC1 baroclinic developments evolved beneath the core of the upper jet, while LC2 developments occured on the cyclonic-shear side of the upper jet [*Shapiro et al.*, 1999]. More evidence of such a relationship has been found over the eastern North Pacific in 1998–1999 by [*Shapiro et al.*, 2001]. They further suggest that anomalies in the time-mean ambient flow associated during La Niña and El Niño episodes lead to preferential life cycles that mimic the LC1 and LC2 paradigms, respectively.

[7] The aim of the paper is, therefore, to provide a typology of precipitating systems over the North Atlantic Ocean during wintertime and to examine the potential relationship between individual precipitating systems and low-frequency variability. The latter is characterized here through two concepts, both based on the geopotential height field analysis: the Arctic Oscillation (AO), the leading mode of the Northern Hemisphere sea level pressure variability [*Thompson and Wallace*, 1998], and the weather regimes, defined as recurrent climate patterns obtained by clustering methods [*Vautard et al.*, 1988]. In addition, the response of El Nino Southern Oscillation (ENSO) warm and cold extremes in terms of characteristics of precipitating systems is examined, since some authors have related the cyclone activity over this area with ENSO phases [e.g., *Sickmöller et al.*, 2000]. The paper is arranged as follows: Section 2 presents the data and the classification method. In section 3 the results of the classification method are discussed. In section 4, the relationship between precipitating systems and low-frequency variability is investigated. Section 5 provides a summary.

2. Data and Method

2.1. Satellite Data

[8] Observations used for this study are from NOAA-10 and NOAA-12 satellites for nine northern winters (December–February, DJF, with the exception of December 1986) from January 1987 to February 1995. The TOVS radiometer, which flies on-board the NOAA satellites mainly consists of two instruments: High Resolution Infrared Radiation Sounder (HIRS-2) and microwave sounding unit (MSU). HIRS-2 is a radiometer with 19 channels in the infrared band and one in the visible band and its spatial resolution is about 17 km at nadir. MSU is a four-channel passive microwave radiometer for which the horizontal resolution is ranging from 110 km at nadir to 323 km at the edges of the swath. The raw TOVS data have been converted into atmospheric parameters using the Improved Initialization Inversion algorithm [*Chédin et al.*, 1985; *Scott et al.*, 1999]. Among a large number of variables, this physicostatistical method, relying on pattern recognition approach, determines the temperature of lower stratosphere (TLS), the cloud top pressure, and a precipitation index. All these variables are retrieved at a spatial resolution of 100 km by 100 km every 12 hours at best.

[9] TLS is used to describe the thermal structures at the tropopause level [*Fourrié et al.*, 2000]. TLS is obtained through a combination of brightness temperatures from five TOVS channels (HIRS 2 and 3 and MSU 2, 3, and 4) weighted by a set of regression coefficients. These TOVS channels are the most sensitive to the temperature around the tropopause. While MSU3 plays the major role, the other channels are also significant. As a consequence, TLS fields show more variability than the raw MSU3 data alone. As shown through quantitative comparisons with model analysis, TLS is a good indicator of the averaged temperature between the 4 and 8 PVU (potential vorticity unit, 1 PVU = 10^{-6} K m^2 s^{-1} kg^{-1}) levels (i.e., in the layer 1–4.5 km above the tropopause). In particular, warm anomalies of TLS can be used to detect upper level precursors of cyclogenesis. Moreover, TLS fields allow to detect other upper level structures such as troughs, ridges,

and tropopause breaks along the cyclonic shear side of an upper level jet [*Fourrié et al.*, 2000, 2003].

[10] In the 3I algorithm, clouds are detected at the HIRS spatial resolution (18 km at nadir) by a succession of seven (night)/eight (day) threshold tests, which depend on the simultaneous MSU radiance measurements probing through clouds. Cloud parameters are determined from the radiances averaged over all cloudy HIRS pixels within the 3I box, assuming a single, homogeneous cloud layer. The average cloud top pressure and the effective cloud amount are obtained by a weighted-χ^2 method from four 15 μm CO_2 band radiances and the 11 μm atmospheric window radiance (HIRS 4 to 8) [*Stubenrauch et al.*, 1999a]. The empirical weights reflect the usefulness of a spectral channel at a cloud level for the determination of the effective cloud amount. A cloud cover fraction is also determined as the fraction of cloudy HIRS pixels in each grid box. The 3I cloud parameters have been evaluated on a global scale [*Stubenrauch et al.*, 1999b] by comparison with time-space collocated, reprocessed ISCCP cloud parameters. The remaining discrepancies with ISCCP can be explained by differences in cloud detection sensitivity, differences in the atmospheric temperatures profiles used, and by inhomogeneous or partly cloudy fields.

[11] In spite of its rather coarse resolution with respect to mesoscale features, the MSU gives valuable information on precipitation which has the advantage to be collocated in time and space with the two preceding geophysical variables, In particular, MSU1 and MSU2 sense upwelling radiation at 50.31 and 53.73 GHz, respectively, with respective peak responses at sea level and 700 hPa. MSU2 has its primary signal due to absorption and emission of thermal radiation by molecular oxygen. In contrast to MSU2, MSU1 experiences large cloud water and surface contributions compared to its air temperature sensitivity. Thus in mid-February 1980 an oceanic precipitation test was introduced operationally by the National Environmental Satellite Service. It consisted of declaring situations contaminated by rain when the brightness temperature difference of MSU2 minus MSU1 is less than 12 K [*Phillips*, 1980]. In the 3I algorithm the same test on MSU data is used, but with a threshold set at 16 K [*Claud et al.*, 1995]. Furthermore, the MSU data are normalized for the effect of scan angle with the help of Special Sensor Microwave/Imager data, yielding the normalized precipitation index ΔMSU [*Chaboureau et al.*, 2001].

2.2. Classification Method

[12] To characterize the variability of precipitating systems, a composite analysis is used. The satellite retrievals are projeted onto a polar stereographic conformal grid with a grid spacing of 120 km × 120 km. The precipitating events are defined by areas covering more than 200,000 km^2 with values of the normalized ΔMSU less than 16 K (a threshold indicator of rain) and characterized by a cloud top pressure less than 400 hPa. They are searched between 40°N–60°N and 70°W–10°W. Then, TLS, cloud top pressure, and normalized ΔMSU fields are extracted in a square of 3600 km side length, centered over the rain event. The orientation of the square is such that the *y* axis is toward the north. To enlarge the view upstream of the rain event, the box is shifted 600 km to the east from the geometric center of the box. Since normalized ΔMSU is also sensitive to low-level temperature variations, only fields of TLS and cloud top pressure are used in the following. Each case is thus represented by a vector of 31 × 31 × 2 = 1922 values. A reduction of space is necessary to classify the cases. A principal component analysis (PCA) is thus performed on the normalized fields of TLS and the cloud top pressure. The latter are projeted onto the components of the first eigenvectors which represent the larger variance. So the PCA yields the ability to select only the pertinent information, that is, the field of variation around their average, and the large-scale structures as described by the first eigenvectors. The mean fields of TLS and cloud top pressure, and the small-scale structures are therefore filtered out. Then, the components kept are clustered using an ascending hierarchical classification, which minimizes the intraclass variance: each case is then included in a class. Finally, composites within each class are build from averaging the original fields (i.e., not the filtered fields described by the first eigenvectors). This yields realistic structures as illustrated below.

3. Results

3.1. Averaged Fields

[13] A total of 525 organized precipitating systems, either fronts or cyclones at different stages of their development, has been obtained using the definition given in the previous subsection. Figure 1 presents the retrievals (the cloud top pressure, TLS, and the precipitation index) averaged over the selected systems and the associated standard deviation. As prescribed, the highest cloud top with a maximum of rain field and a minimum of cloud top pressure standard deviation, less than 120 hPa, is located at the point (0, 0) km. The cloud field is organized toward the northeast with a maximum of TLS field to the west, that is, upstream. Overall, this shows that the averaged precipitating system presents a spatial configuration with the rain maxima downstream the warm TLS pattern, suggesting a baroclinic interaction (or instability) between these lower and upper level features. This result yields a generalization of the one found for the FASTEX 2-month period [*Chaboureau et al.*, 2001]. Moreover, this analysis on precipitating systems, as observed by satellite, agrees with a study on cyclogenesis events which shows that the significant events (i.e., with a deepening greater than 10 hPa per day) always involve a transient baroclinic interaction with some upper level potential vorticity anomaly. This latter study relied on the ECMWF reanalysis of 14 winters [*Ayrault and Joly*, 2000a].

[14] The maximum variability of the cloud field, up to 240 hPa, is found in the south sector, indicating changes in the orientation of the cloud tail from southwest to south (Figure 1b). The TLS field has a maximum of variation in the southwest sector that corresponds to a trough deepening located to the west or the southwest of the cloud center. So the variability appears to be explained by the change in the orientation of the fields of cloud top pressure and TLS, and in the TLS magnitude. It is further explored using the classification method.

3.2. Typology of Precipitating Systems

[15] Table 1 displays the results of the explained variance by the first 10 eigenvectors after the PCA, which is the first

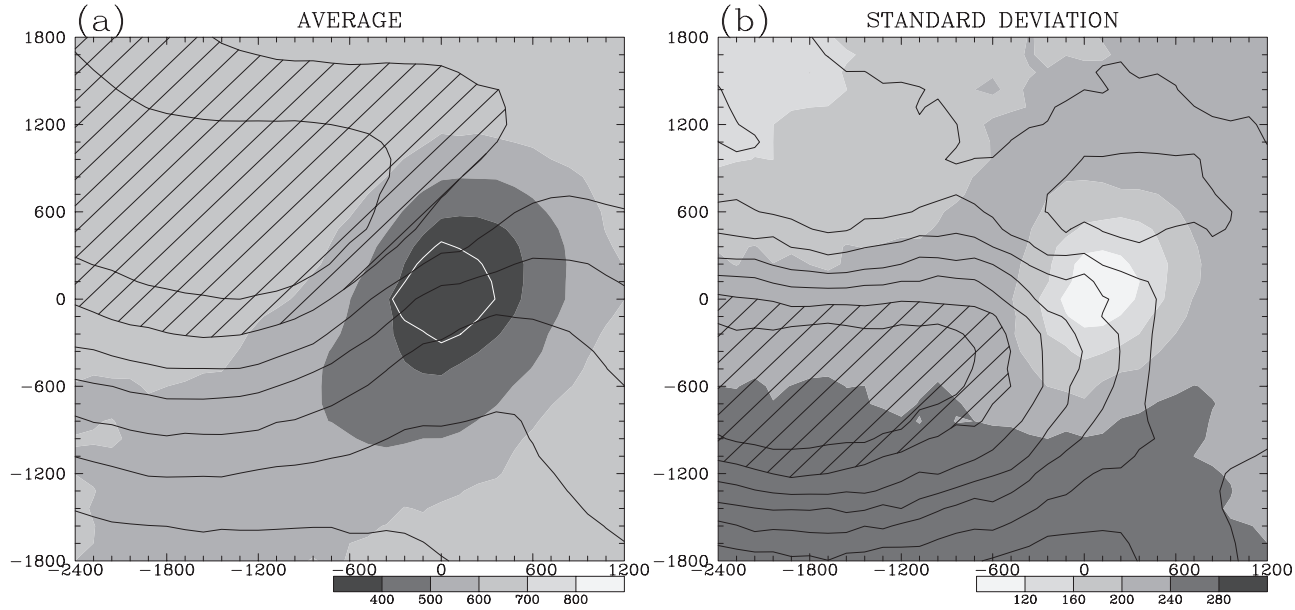

Figure 1. Retrieval fields for cloud top pressure and TLS: (a) averaged over the 525 selected systems and (b) the associated standard deviation. The shading indicates cloud top pressure every 100 hPa in Figure 1a (40 hPa in Figure 1b), the line TLS every 2 K (0.5 K), and the dashed patterns TLS over 218 K (7 K), respectively. In Figure 1a, the white solid line indicates the mean precipitation area (normalized ΔMSU < 16 K).

step of the classification. The first eigenvectors represent the larger variance but are not necessarily representative of all of the cases. On the other hand, the eigenvectors of larger ranks describe less variance, associated with small-scale structures. From Table 1, a right place to separate into informative eigenvectors and useless ones is between the eigenvector of rank 6 and of rank 7: Here there is a large decrease of the explained variance (0.93%) and the first six components represent 44.92% of the total variance. Then, each case projected on the first six components is classified such as minimizing the intraclass variance. The retained classification gives eight classes. Indeed, to be representative, each class should be composed of a large number of individual cases. On the other hand, a too limited number of classes would smooth the variability.

[16] Figure 2 shows the resulting composite views and the number of cases for each class. The latter lies between 20 and 40 cases for classes 1, 2, and 7, around 50 cases for classes 3, 4, and 8, and 89 cases for class 5. Class 6 is the most populated class with 179 cases, that is 34% of the total. As such, its composite fields appear rather similar to the averaged fields. However, if a classification with nine classes had been retained, class 6 would be split into two classes grouping 76 and 103 cases but with composite views also rather similar (not shown). Thus this justifies the compromise obtained with eight classes.

[17] All classes are characterized by the presence of a precipitation area covered by high-level clouds as already seen when examining the averaged fields in Figure 1a. On the other hand, large variability between composites is observed according to the orientation of the cloud system, the tilting and the magnitude of the TLS field. Cloud systems are organized in the zonal direction (class 1), or with a slight tilt toward northeast (classes 2–4), to a more pronounced one (classes 5–7), or even in a south-north direction (class 8). The cloud composites also differ according to the spread of high clouds, as seen by the cloud top pressure less than 500 hPa. Cloud systems of classes 3–5 are confined to a range of 1000 km, while the others extend over a 3000 km range. The warm TLS pattern, as defined as the area where TLS is larger than 218 K, varies from class to class in terms of magnitude and orientation. The warm TLS pattern is confined to the northwest corner (classes 1 and 2) or the central western part (class 5), while it extends all over the northern part (classes 3, 4, and 6) and the western part (classes 7 and 8). Moreover, almost all classes (1–6) show a warm TLS pattern in the zonal direction, while classes 7 and 8 are characterized by the warm TLS tilted anticyclonically and cyclonically, respectively.

[18] Following the results of *Chaboureau et al.* [2001] in the context of FASTEX, class 1 can be associated with zonally elongated cold fronts, classes 3–5 with frontal

Table 1. Results of the Principal Component Analysis Applied to the Selected TLS–Cloud Top Pressure Systems for the First 10 Eigenvectors

Rank	Explained Variance, %	Summation, %	Difference With the Variance Explained by the Next Rank %
1	16.58	16.58	6.35
2	10.24	26.82	4.74
3	5.50	32.32	0.88
4	4.62	36.94	0.43
5	4.19	41.13	0.41
6	3.78	44.92	0.93
7	2.85	47.76	0.12
8	2.73	50.49	0.48
9	2.25	52.74	0.19
10	2.06	54.81	0.29

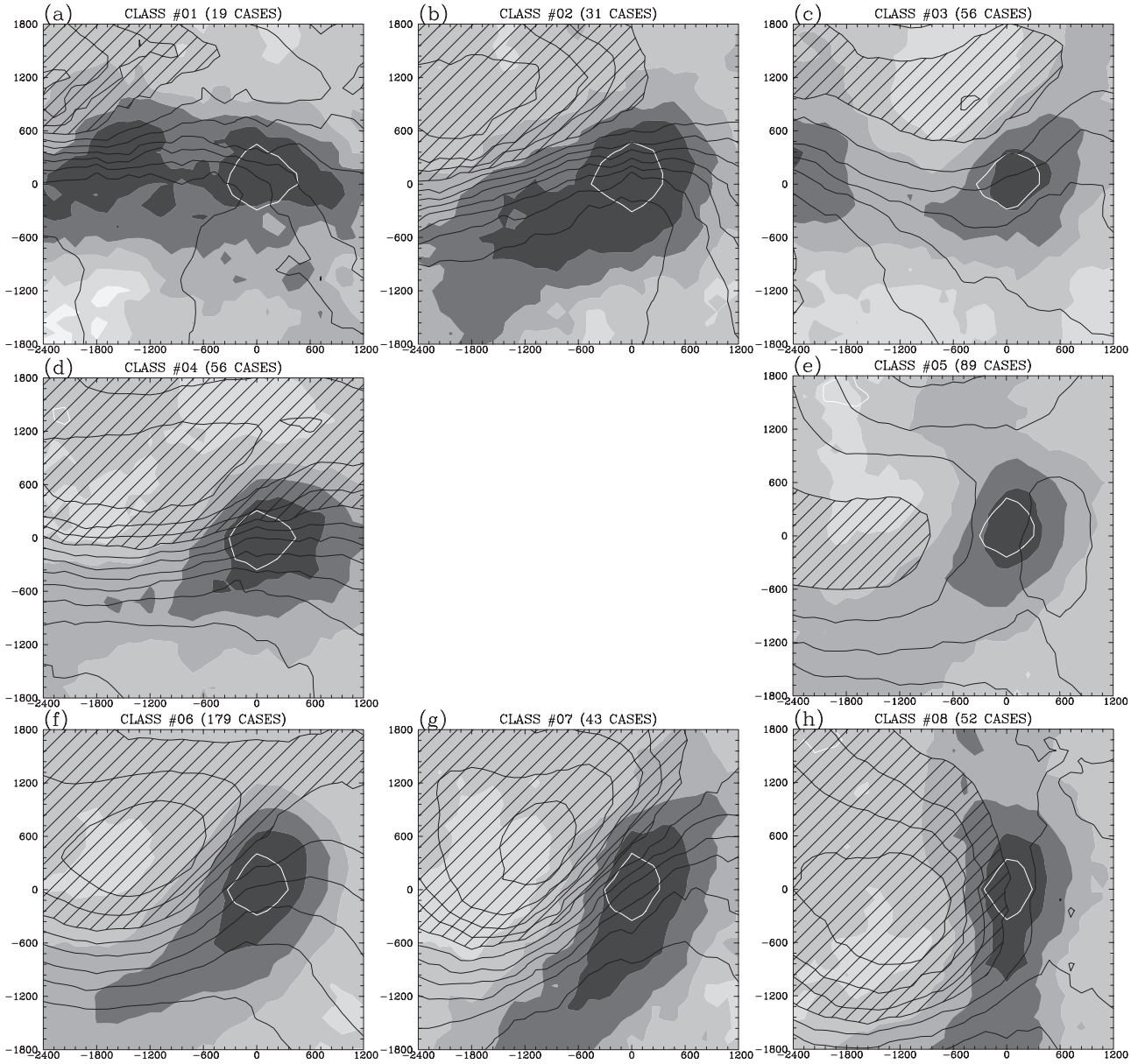

Figure 2. Composite views of the eight classes resulting from the hierarchical classification minimizing the intraclass variance using the first six PCA components. Same plotting convention as in Figure 1a.

waves or end-of-storm track cyclones, and classes 2 and 6 with large-scale fronts or baroclinic systems. Class 7 exhibits an anticyclonically tilted warm TLS pattern and beneath, away from the rain center, an anticyclonically tilted and 1000 km long warm front and a cyclonically tilted and 2000 km long cold front. As such, class 7 mimic the LC1 paradigm at its mature stage when some air turns anticyclonically and equatorward [*Thorncroft et al.*, 1993]. On the other hand, class 8 displays a cyclonically tilted warm TLS pattern, and a cloud shield turning cyclonically over the cold and warm fronts. This suggests that class 8 is typical of the Norwegian cyclones that mimic the LC2 example. Note that the precipitating cyclones can significantly change shape during their life cycle. In their early stage, the idealized LC1 and LC2 both display cyclonic curvature and may look like class 2 or 4 for example: the present cluster analysis can not distinguish between them. This is due to the identification of classes 7 and 8 to LC1 and LC2 paradigms that is made during their mature stage only, when the planetary flow has a significant impact.

[19] Classes 7 and 8 all together represent only a small fraction of the selection (20%). The LC1 and LC2 scenarios are paradigms of the baroclinic-wave life cycle behavior only, while the mechanisms involved in the development of the extratropical cyclones are much more various. This gives further evidence that the climatological reality departs significantly from the idealized situations studied so far in the theoretical literature, as claimed by *Ayrault and Joly* [2000b].

[20] As a conclusion, the composite analysis yields over the selected precipitating systems eight classes that significantly differ in the composite views of cloud top pressure and TLS, their pattern, their magnitude, and the relative locations of the two fields. We now examine whether these

composites present preferential occurrences in space and time.

3.3. Distribution With Space and Time

[21] The normalized frequency distributions of precipitating events with latitude and longitude give insight into the classification (Figure 3, for each class, the frequency of distribution is normalized with respect to the total per class). The distribution per latitude specifies classes 1–4 that group events preferentially found in the southern part of the selection domain (to the south of 45°N), classes 5 and 8 in the northern part, and classes 6 and 7 in between. The distribution per longitude identifies class 4 events from the western part, those of class 5 and 8 from the eastern part, and the remaining classes without any preferential meridional domain. This indicates that the classes, characterized by significantly different composite patterns, also show preferential locations. Classes 1–4, displaying cloud system and warm TLS pattern in a zonal orientation, occur mostly in the southern part (to the south of 45°N). Class 1 can be associated with zonal cold fronts, class 2 with large-scale frontal systems, and classes 3 and 4 with frontal waves. On the other hand, the most tilted composite fields (classes 5–8) are found either in the central mid-Atlantic (classes 6 and 7) or to the northeast (classes 5 and 8), near the exit of the storm track. Class 5 groups end-of-storm track cyclones, class 6 is populated with large-scale fronts or baroclinic systems, and classes 7 and 8, that mimic LC1 and LC2, are found toward the exit of storm track, in the central and the northeast Atlantic, respectively.

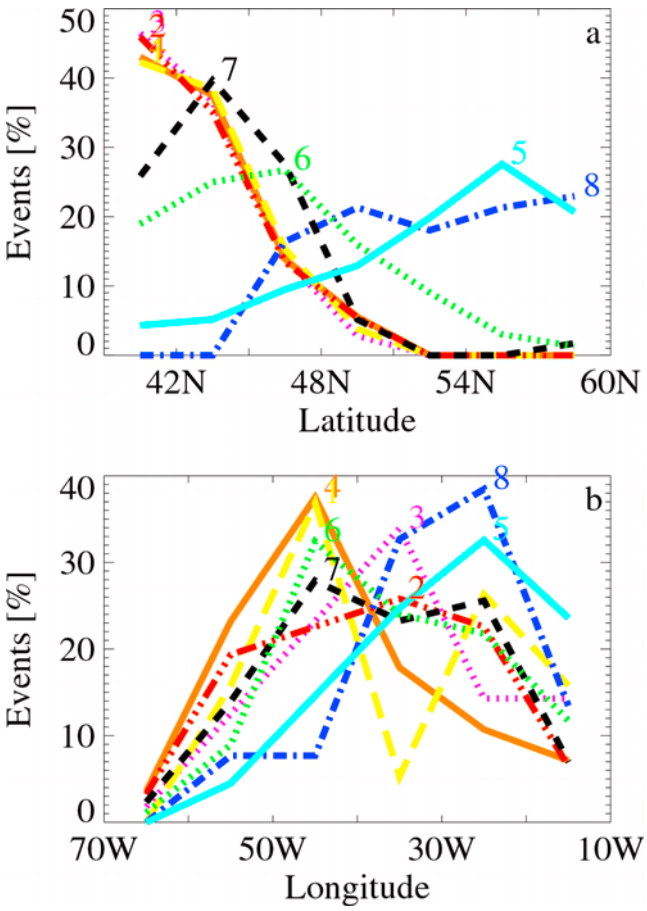

Figure 3. Normalized frequency distributions for each of the eight classes showing the percentage of cloud system events per (a) latitude and (b) longitude. The class numbers are written close to the maximum percentage of events.

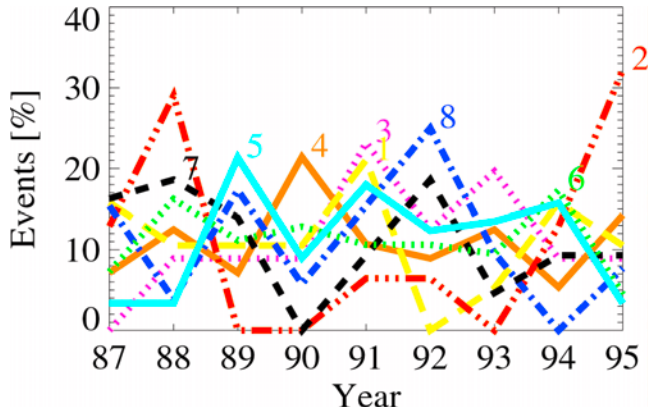

Figure 4. Normalized frequency distributions for each of the eight classes showing the percentage of cloud system events per year. Same plotting convention as in Figure 3.

[22] Finally, in a consistent way, the associated precipitating center of classes 5–8 is more to the north than the warm TLS pattern, compared to classes 1–4. This shows that most of the precipitating systems belonging to classes 5–8, also at a well developed stage, are more sensitive to the orientation of the upper level feature when traveling in the western part of the Atlantic basin than the precipitating systems from classes 1–4.

[23] Figure 4 presents the normalized frequency distributions of precipitating events as function of year. Large interannual variability can be observed: For example, concerning class 2, events are found mostly in 1988 and 1992, and none in 1989, 1990, and 1993; for class 8, the distribution ranges from 0 (in 1994) and 25% (in 1992); there is no event belonging to class 1 in 1992, and about 20% of the cases are found in 1991; this is also true for class 3 (0% in 1987 and more than 20% in 1991); class 7 exhibits two peaks at about 18% in 1988 and 1992 but is not represented in 1990. In contrast with this large interannual variability per class, the total number of rain events is the same each year with about 60 events.

4. Relationship Between Precipitating Systems and Low-Frequency Variability

[24] In order to understand the large interannual variability of the classes found in the previous section, the relationship between precipitating systems and the low-frequency variability is now investigated using two different ways to describe it, the AO and the weather regimes. The distribution of the precipitating systems during ENSO warm and cold extremes is also examined.

4.1. Low-Frequency Variability: AO and Weather Regimes

[25] The low-frequency variability in the Northern extratropics is often described by the leading empirical orthogonal function of the sea level pressure (SLP) or the

geopotential field. Two indices are largely used, the North Atlantic Oscillation (NAO) and the AO. Although the NAO is specific to the Atlantic basin and the AO address the whole Northern Hemisphere variability, the NAO and AO are found arguably inseparable during winter by *Rogers and McHugh* [2002]. The index used here is the daily AO index generated by projecting the leading empirical orthogonal function of SLP poleward of 20°N onto daily SLP anomalies, based on NCEP/NCAR reanalysis from January 1958 to April 1997 [see *Thompson and Wallace*, 2000]. However, considering the NAO daily index instead of the AO index would lead to similar results. After *Hurrell* [1995], during the positive NAO phase, precipitating systems follow a more southwest-to-northeast track. Conversely, during the negative NAO phase, the precipitating systems follow a west-east storm track.

[26] Another way to describe the low-frequency variability is through the concept of weather regime, a dynamically equilibrated pattern corresponding to quasi-steady persistent weather as defined by *Vautard et al.* [1988]. For the period of interest in this study, a regime identification based on the 700 hPa geopotential field of the four-daily analyses produced by ECMWF has been performed by *Ayrault et al.* [1995]. This has led to four regimes: the zonal (ZO), blocking (BL), Greenland Anticyclone (GA) and Atlantic ridge (AR) regimes. The ZO regime corresponds to a maximum eastward penetration of the zonal jet, associated with a low centered over northern Europe extending upstream to Greenland. The BL is characterized by the jet confined to the western part of the Atlantic and a block located over western Europe. The GA regime corresponds to an anticyclone over Greenland and the polar jet moved southward, by reference to its ZO regime position, almost in continuity with the African subtropical jet. This gives a zonally symmetric pattern to its southern part. The AR regime is characterized by a ridge over the mid-eastern Atlantic, bringing over Europe moist cold air advected from the northern Atlantic.

[27] Although many investigators have examined the AO and weather regimes separately, few have explored the statistical and dynamical relationship between them in a unified manner. (An exception comes from *Shabbar et al.* [2001], who have examined NAO and blocking episodes only.) Figure 5 presents the temporal evolution of the daily AO index and of the weather regimes for the years from 1987 to 1994, and in 1995 for the AO index only. The selected precipitating systems are also indicated by the "x" symbol on the $y = 0$ line. They are found in similar proportion each winter, but are missing during periods of few days (e.g., between days 30 and 40 in 1994). This may come from the case selection which is made on large oceanic precipitating events only.

[28] The AO index fluctuates on timescales of about 10 days, consistently with the findings of *Feldstein* [2000]. It is often positive, with an average of 0.7, and almost always positive for winters 1989, 1991, 1992, and 1993. The persistence of weather regimes is variable, from 3 days up to 50 days. The AR regime is only just present few days in December 1991, 1993, and 1994, while the ZO regime occurs during long periods in 1988, 1990, and 1994, for example. BL and ZO regimes are the most interpenetrated (e.g., in 1989) due to their similarities over western Atlantic (they differ over western Europe).

[29] Interestingly, the BL and ZO regimes occur preferentially during the positive AO phases, while the GA regime is often associated with negative AO values. The GA regime, characterized by a weaker polar jet stream and a stronger subtropical jet stream [see *Ayrault et al.*, 1995], matches well the negative AO phase and the related reduced meridional pressure gradient resulting in a more west-east storm track. In a similar way, the polar jet is strengthened during the ZO regime which is consistent with the classical view of the positive AO phase. Finally, although the polar jet is confined to western Atlantic during the BL regime, the jet is strong enough to associate the BL regime with the positive AO phase.

4.2. Precipitating System Distribution With AO Phase

[30] In order to relate high-frequency to the low-frequency variability, composites of extreme AO phases have been built (Figure 6). Negative ($AO < -1$) and positive ($AO > 2.5$) composites group together 48 cases. The negative AO composite displays a compact cloud cover and a warm TLS field restricted to the northwest quarter, while the positive AO composite shows a cloud cover elongated toward the northeast and a zonally undulation of the warm TLS field. (The associated standard deviation fields (not shown) display structures similar to those displayed in Figure 1b.) This different structure of the composite fields indicates that the AO has an impact on the distribution of the systems. We now examine the influence of the AO phase, class by class.

[31] Figure 7 presents the distributions of precipitating events is now examined as a function of the daily AO index. When examining the most tilted composite fields (classes 5–8), there is no specific discrimination with AO. These classes display a bell distribution peaking between 0 and 2 and spreading over the full range of the AO index. On the contrary, the classes with the most zonal orientation (classes 2–4) which mainly group events found to the south of 45°N display an AO preference. Most of class 2 events characterized by a 3000-km-wide cloud pattern are found for a negative AO (between −1 and 0), while classes 3 and 4 with a 1000-km-wide cloud system correspond to a positive AO index (around 1). This indicates that a weak (strong) jet flow regime favors the zonally elongated precipitating systems to be largely (weakly) developed to the south of 45°N.

4.3. Precipitating System Distribution With Weather Regimes

[32] The normalized frequency distributions of precipitating events is now examined as a function of weather regime (Figure 8). When focusing on the classes with the most zonal orientation (classes 1–4), it leads to the conclusion that classes 3 and 4 mainly group events found during the ZO regime (over 60%) which corresponds to a positive AO index, consistently with the association between ZO regime and positive AO phase. In a similar way, class 2 groups a large proportion of events (40%) from GA regimes, that occur mostly during negative AO phase. Results are consistent with the statements of the previous subsections. However, other 40% of class 2 events occur during ZO regimes, indicating a non-univocal relationship between classes, AO phase, and weather regimes.

[33] When examining the most tilted composite fields (classes 5–8), they group precipitating events found mostly

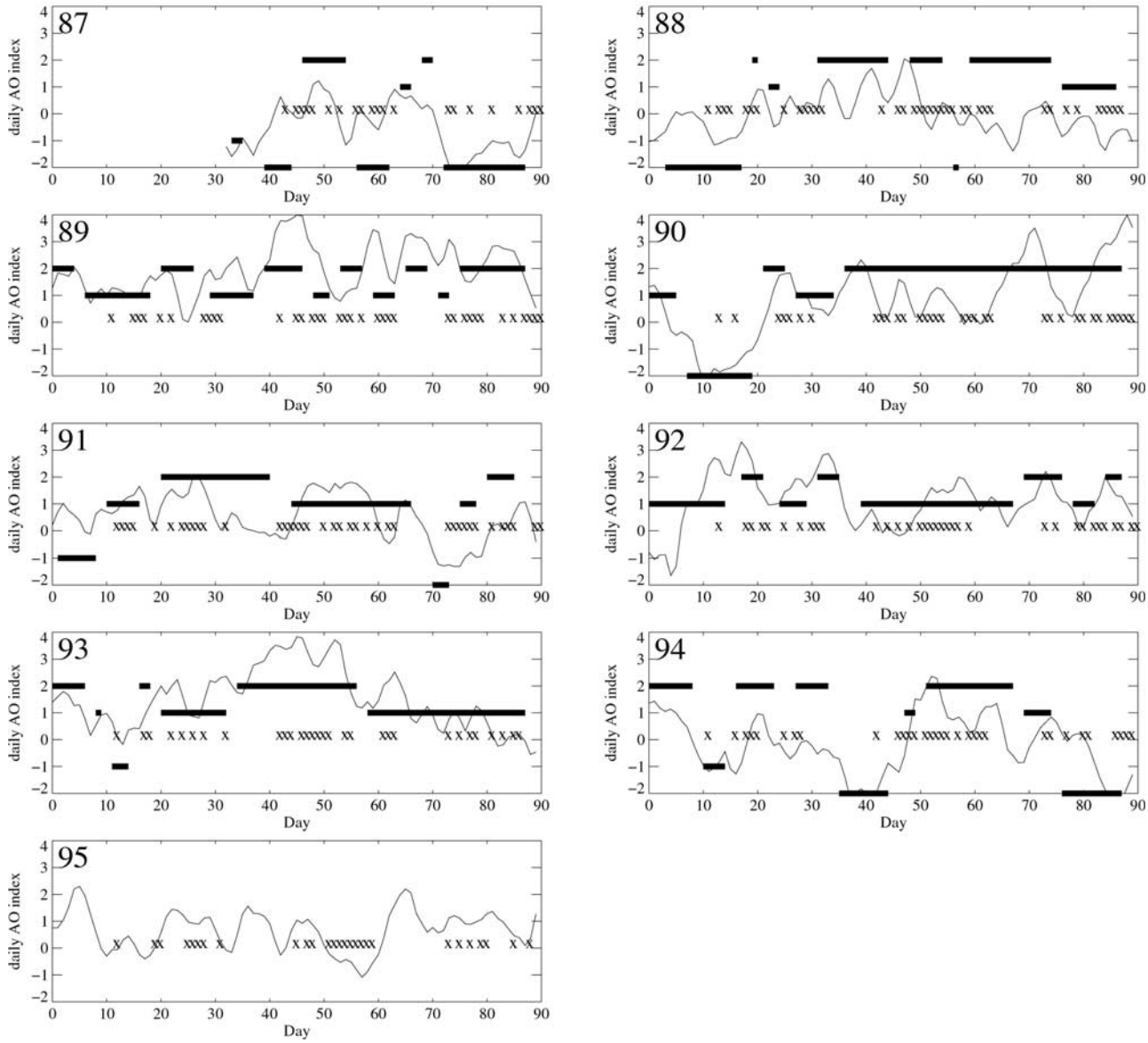

Figure 5. Temporal evolution of the AO index (thin line) and of the weather regimes (thick line) for the years from 1987 to 1994 and in 1995 for the AO index only. The GA, AR, BL, and ZO regimes values are indicated by y values of −2, −1, 1, and 2, respectively. Days begin on 1 December and end at 28 February of the following year. Years are labeled on January of the period. Each "x" on the $y = 0$ line represents a selected precipitating system.

during the ZO and BL regimes, at least more than 35% in each case. In particular, classes 7 and 8, the LC1 and LC2 types, are favored during the BL regime, with frequencies of 50 and 60%, respectively. The anticyclone located over eastern Atlantic results in the splitting of the storm track into two paths, one northeastern and the other southeastern as shown by *Hoskins et al.* [1983] and illustrated during FASTEX by *Baehr et al.* [1999]. Consistently, class 7 is found preferentially to the south, that is, to the anticyclonic side of the jet. Similarly, class 8 occurs to the northeast, the cyclonic side of the jet. These systems are cyclonically tilted in the northeastern branch of the storm track and anticyclonically tilted in the southwestern branch. This analysis gives observational evidence of previous idealized simulations linking the large-scale circulation to preferential life cycles of weather systems.

4.4. Relationship With ENSO

[34] The potential impact of warm and cold ENSO phases on cyclone activity over the North Atlantic has been discussed in particular by *Fraedrich et al.* [1992] and *Palmer and Anderson* [1994]. *Fraedrich et al.* [1992], using a catalogue of 86 years of daily circulation patterns, show an influence of the ENSO extremes on the zonality in the winters which follow the year of the event. Using reanalyzed ECMWF data, *Sickmöller et al.* [2000] show that the preferred regions of cyclone occurrence change with the ENSO phase and that propagating cylones occur less and stationary ones occur more frequently during El Niño warm-

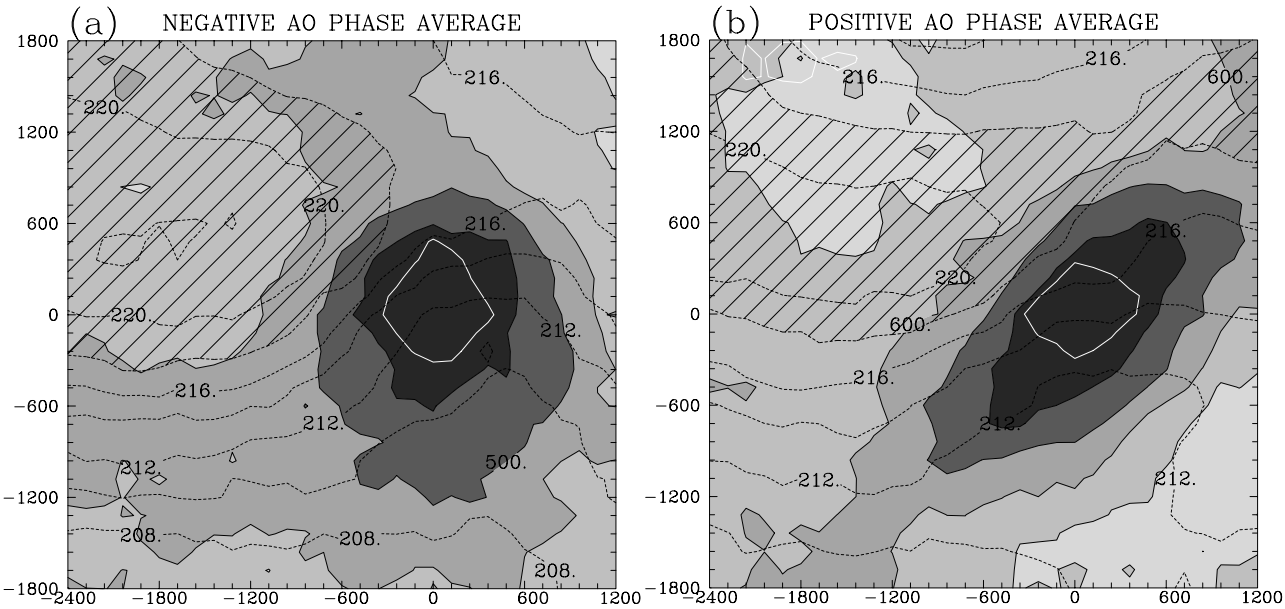

Figure 6. Composite views for the subsets of (a) negative AO phase and (b) positive AO phase. Same plotting convention as in Figure 1a.

event winters. Composites of extreme ENSO phases have therefore been built using the NINO3.4 index obtained from the Climate Prediction Center (NOAA) and are presented in Figure 9. Negative (NINO3.4 < −1.5) and positive (NINO3.4 > 2.5) composites group together 45 cases during winter 1989 and 65 cases during winter 1992, respectively. It shows no evidence of any relationship between ENSO and the structure of the composite systems. In terms of location, cases corresponding to a positive index are slightly more numerous around 40°W and in the southern part of the area of interest (not shown), which is consistent with the results of *Sickmöller et al.* [2000], but the response remains weak.

5. Summary

[35] The observed variability of large oceanic precipitating systems in the North Atlantic during winter is investigated using polar satellite data covering the period 1987–1995. While almost all the studies devoted to this issue are done using reanalyses, this approach is based on satellite observation and is therefore novel. The precipitating systems are detected automatically, using consistent (i.e., temporally and spatially collocated) retrievals of cloud top pressure, a precipitation index, and the temperature of the lower stratosphere. This leads to a generalization of the results of [*Chaboureau et al.*, 2001], which was conducted over the FASTEX two-month period, and showed that the variability of these systems could be described using the three preceding variables. A classification of the systems was then conducted. The eight resulting classes significantly differ in structure, and are associated with frontal waves, zonal cold fronts, and large-scale frontal or baroclinic systems. In particular, two classes are identified because of the tilt of their shape as LC1 and LC2 paradigms. It also

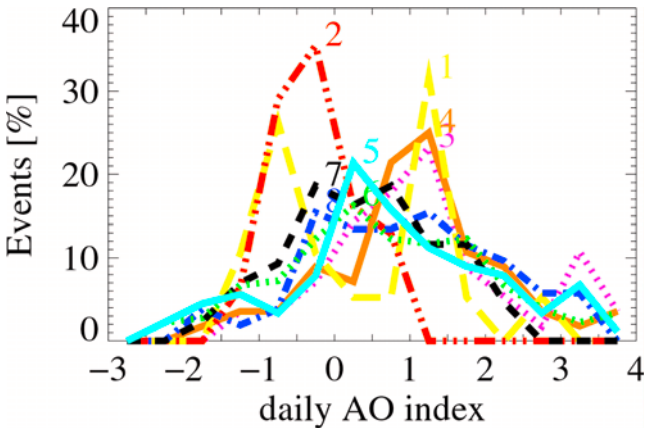

Figure 7. Normalized frequency distributions for each of the eight classes showing the percentage of cloud system events per daily AO index. Same plotting convention as in Figure 4.

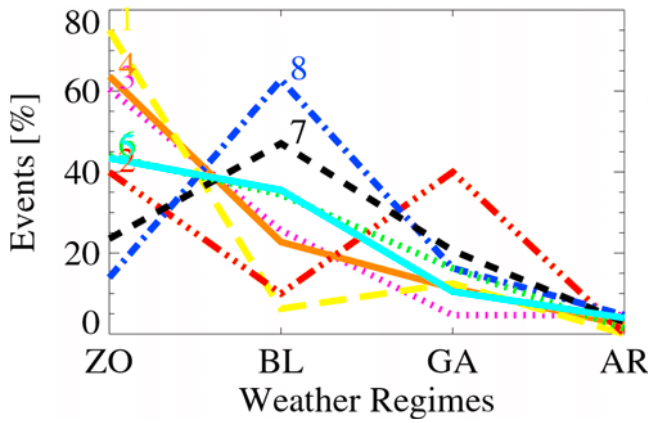

Figure 8. Normalized frequency distributions for each of the eight classes showing the percentage of cloud system events per weather regime. Same plotting convention as in Figure 4.

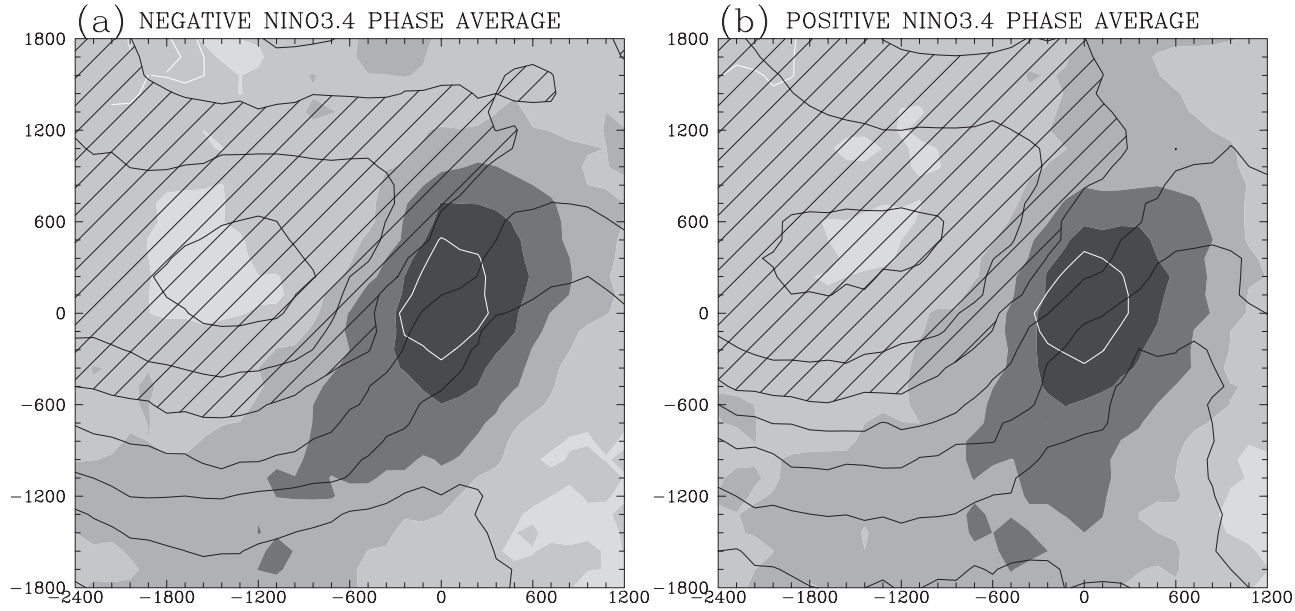

Figure 9. Composite views for the subsets of (a) negative NINO3.4 phase and (b) positive NINO3.4 phase. Same plotting convention as in Figure 1a.

shows the systematic presence of a trough upstream the precipitating area covered by high-level clouds, as expected in case of baroclinic interaction.

[36] The occurrence of the classes differs significantly depending on the years. In order to understand this large interannual variability, an attempt to identify systematic differences in cyclone structures during different flow regimes was then performed. Two concepts were considered to characterize the regimes: first the AO/NAO concept, and then the weather regimes concept. The distribution of the eight classes with each of the concepts was studied, but also the correspondence between the two concepts. Results were found independent of the index (AO or NAO). The BL and ZO regimes occur preferentially during the positive AO phases, while the GA regime is often associated with negative AO values.

[37] Furthermore, large-scale (typically 3000 km wide) and zonally elongated cloud systems are observed mainly to the south of 45°N when the phase of the AO is negative (which also corresponds to the GA regime). Conversely, zonally elongated cloud systems of smaller scale (1000 km wide) associated with frontal waves are favored also to the south, but during the positive AO phase (particularly during ZO regimes). The most tilted weather systems, without any preferential AO phase, are found mostly during the BL regime: the LC2 cyclonically tilted systems are in the northeastern branch of the storm track and the LC1 anticyclonically tilted ones in the southwestern branch. This analysis gives observational evidence of previous idealized simulations linking the large-scale circulation to preferential life cycles of weather systems.

[38] In addition, the relationship between ENSO and the structure of the composite systems has been investigated. This was motivated by earlier studies which showed a significant, although generally rather weak, response of cyclonic activity over the North Atlantic during wintertime to ENSO. On the basis of this nine-winter satellite data set, a weak response to extreme ENSO events has been observed in the location of cyclones but not in their average structure.

[39] The use of satellite data to study the variability of storms remains largely unexplored. We plan to pursue this work by investigating other storm tracks over a longer period of time (using reanalyzed TOVS data available since 1979).

[40] **Acknowledgments.** Retrievals used here have been obtained from the Atmospheric Radiation Analysis group at LMD, through the NOAA/NASA TOVS Pathfinder (Path-B) program. We are grateful to the anonymous reviewers for the constructive comments.

References

Ayrault, F., and A. Joly, Une nouvelle typologie des dépressions météorologiques, classification des phases de maturation, *C. R. Acad. Sci., Ser. IIa Sci. Terre Planetes*, *330*, 167–172, 2000a.

Ayrault, F., and A. Joly, L'origine des dépressions météorologiques sur l'atlantique: Nouvelle perspective climatologique, *C. R. Acad. Sci., Ser. IIa Sci. Terre Planetes*, *330*, 173–178, 2000b.

Ayrault, F., F. Lalaurette, A. Joly, and C. Loo, North Atlantic ultra high frequency variability, *Tellus, Ser. A*, *47*, 671–696, 1995.

Baehr, C., B. Pouponneau, F. Ayrault, and A. Joly, Dynamical characterization of the FASTEX cyclogenesis cases, *Q. J. R. Meteorol. Soc.*, *125*, 3469–3494, 1999.

Chaboureau, J.-P., C. Claud, J.-P. Cammas, and P. Mascart, Large-scale cloud, precipitation, and upper level features during FASTEX as inferred from TOVS observations, *J. Geophys. Res.*, *106*, 17,293–17,302, 2001.

Chédin, A., N. A. Scott, C. Wahiche, and P. Moulinier, The improved initialization inversion method: A high resolution physical method for temperature retrievals from the TIROS-N series, *J. Clim. Appl. Meteorol.*, *24*, 124–143, 1985.

Claud, C., K. B. Katsaros, N. M. Mognard, and N. A. Scott, Synergetic satellite study of a rapidly deepening cyclone over the Norwegian Sea: 13–16 February 1989, *Global Atmos. Ocean Syst.*, *3*, 1–34, 1995.

Davies, H. C., C. Shär, and H. Wernli, The palette of fronts and cyclones within a baroclinic wave development, *J. Atmos. Sci.*, *48*, 1666–1689, 1991.

Evans, M. S., D. Keyser, L. F. Bosart, and G. M. Lackmann, A satellite-derived classification scheme for rapid maritime cyclogenesis, *Mon. Weather Rev.*, *122*, 1381–1416, 1994.

Feldstein, S. B., The timescale, power spectra, and climate noise properties of teleconnection patterns, *J. Clim.*, *13*, 4430–4440, 2000.

Fourrié, N., C. Claud, J. Donnadille, J.-P. Cammas, B. Pouponneau, and N. A. Scott, The use of TOVS observations for the identification of tropopause-level thermal anomalies, *Q. J. R. Meteorol. Soc.*, *126*, 1473–1494, 2000.

Fourrié, N., C. Claud, and A. Chédin, On the depiction of upper-level precursors of the December 1999 storms from TOVS observations, *Weather Forecasting*, *18*(3), 417–430, 2003.

Fraedrich, K., K. Müller, and R. Kuglin, Northern hemisphere circulation regimes during the extremes of the El Niño/Southern Oscillation, *Tellus, Ser. A*, *44*, 33–40, 1992.

Geng, Q., and M. Sugi, Variability of the North Atlantic cyclone activity in winter analyzed from NCEP-NCAR reanalysis data, *J. Clim.*, *14*, 3863–3873, 2001.

Hoskins, B. J., Theory of extratropical cyclones, in *Extratropical Cyclones, Palmén Memorial Volume*, edited by C. W. Newton and E. O. Holopainen, pp. 63–80, Am. Meteorol. Soc., Boston, Mass., 1990.

Hoskins, B. J., and K. I. Hodges, New perspectives on the Northern Hemisphere winter storm tracks, *J. Atmos. Sci.*, *59*, 1041–1061, 2002.

Hoskins, B. J., I. N. James, and G. H. White, The shape, propagation and mean-flow interaction of large-scale weather systems, *J. Atmos. Sci.*, *40*, 1595–1612, 1983.

Hurrell, J., Decadal trends in the North Atlantic Oscillation: Regional temperature and precipitation, *Science*, *269*, 676–679, 1995.

Lau, N.-C., and M. W. Crane, A satellite view of the synopic-scale organization of cloud properties in midlatitude and tropical circulation systems, *Mon. Weather Rev.*, *123*, 1984–2006, 1995.

Paciorek, C. J., J. S. Risbey, V. Ventura, and R. Rosen, Multiple indices of Northern Hemisphere cyclone activity, winters 1949–99, *J. Clim.*, *15*, 1573–1590, 2002.

Palmer, T. N., and D. L. T. Anderson, The prospects for seasonal forecasting—A review paper, *Q. J. R. Meteorol. Soc.*, *120*, 755–793, 1994.

Phillips, N. A., Cloudy winter satellite retrievals over the extratropical Northern Hemisphere oceans, *Mon. Weather Rev.*, *109*, 652–659, 1980.

Rogers, J. C., and M. J. McHugh, On the separability of the North Atlantic Oscillation and Arctic Oscillation, *Clim. Dyn.*, *19*, 599–608, 2002.

Scott, N. A., A. Chédin, R. Armante, J. Francis, C. J. Stubenrauch, J.-P. Chaboureau, F. Chevallier, C. Claud, and F. Chéruy, Characteristics of the TOVS Pathfinder Path-B dataset, *Bull. Am. Meteorol. Soc.*, *80*, 2679–2702, 1999.

Shabbar, A., J. Huang, and K. Higuchi, The relationship between the wintertime North Atlantic Oscillation and blocking episodes in the North Atlantic, *Int. J. Climatol.*, *21*, 355–369, 2001.

Shapiro, M. A., H. Wernli, J.-W. Bao, J. Methven, X. Zou, J. Doyle, T. Holt, E. Donall-Grell, and P. Neiman, A planetary-scale to mesoscale perspective of the life cycles of extratropical cyclones: The bridge between theory and observations, in *The Life Cycles of Extratropical Cyclones*, edited by M. A. Shapiro and S. Gronas, pp. 139–186, Am. Meteorol. Soc., Boston, Mass., 1999.

Shapiro, M. A., H. Wernli, N. A. Bond, and R. Langland, The influence of the 1997–1999 ENSO on extratropical baroclinic life cycles over the eastern North Pacific, *Q. J. R. Meteorol. Soc.*, *80*, 331–342, 2001.

Sickmöller, M., R. Blender, and K. Fraedrich, Observed winter cyclone tracks in the Northern Hemisphere in re-analysed ECMWF data, *Q. J. R. Meteorol. Soc.*, *126*, 591–620, 2000.

Stubenrauch, C. J., A. Chédin, R. Armante, and N. A. Scott, Clouds as seen by infrared sounders (3I) and imagers (ISCCP), II, A new approach for cloud parameter determination in the 3I algorithms, *J. Clim.*, *12*, 2214–2223, 1999a.

Stubenrauch, C. J., W. B. Rossow, F. Chéruy, A. Chédin, and N. A. Scott, Clouds as seen by infrared sounders (3I) and imagers (ISCCP), I, Evaluation of cloud parameters, *J. Clim.*, *12*, 2189–2213, 1999b.

Thompson, D. W. J., and J. M. Wallace, The Arctic Oscillation in the wintertime geopotential heigh and temperature fields, *Geophys. Res. Lett.*, *25*, 1297–1300, 1998.

Thompson, D. W. J., and J. M. Wallace, Annular modes in the extratropical circulation. part I: Month-to-month variability, *J. Clim.*, *13*, 1000–1016, 2000.

Thorncroft, C. D., B. J. Hoskins, and M. E. McIntyre, Two paradigms of baroclinic-wave life-cycle behavior, *Q. J. R. Meteorol. Soc.*, *119*, 17–55, 1993.

Vautard, R., B. Legras, and M. Déqué, On the source of midlatitude low-frequency variability. part I: A statistical approach to persistence, *J. Atmos. Sci.*, *45*, 2811–2844, 1988.

Wernli, H., R. Fehlmann, and D. Lüthi, The effect of barotropic shear on upper-level induced cyclogenesis: Semigeostrophic and primitive equation numerical simulations, *J. Atmos. Sci.*, *55*, 2080–2094, 1998.

J.-P. Chaboureau, Laboratoire d'Aérologie, Observatoire Midi-Pyrénées, 14 av. E. Belin, 31400 Toulouse, France. (chajp@aero.obs-mip.fr)

C. Claud, Laboratoire de Météorologie Dynamique, École Polytechnique, Palaiseau, France.